IUCrJ

Volume 4 (2017)

Supporting information for article:

Coherent amplification of X-ray scattering from meso-structures

Julien R. Lhermitte, Aaron Stein, Cheng Tian, Yugang Zhang, Lutz Wiegart, Andrei Fluerasu, Oleg Gang and Kevin G. Yager

Coherent Amplification of X-ray Scattering from Meso-structures

Julien Lhermitte,[a] Aaron Stein,[a] Cheng Tian,[a] Yugang Zhang,[b] Lutz Wiegart,[b] Andrei Fluerasu,[b] Oleg Gang[a,c,d] and Kevin G. Yager [a]*

[a] *Center for Functional Nanomaterials, Brookhaven National Laboratory, Upton, New York 11973 US,* [b] *National Synchrotron Light Source II, Brookhaven National Laboratory, Upton, New York 11973 US,* [c] *Department of Chemical Engineering, Columbia University, New York, NY, 10027, USA US, and* [d] *Department of Applied Physics and Applied Mathematics, Columbia University, New York, NY, 10027 US.*

E-mail: kyager@bnl.gov

1. Intuitive explanation of the boost factor

To gain a better understanding, one can also examine the noise terms separately: $\sigma_{s/a/bg} = \sqrt{I_{s/a/bg}}$. Assuming the criterion is $C_{req} = 1$, then the signal must exceed each of these noise values. Figure 1 schematically represents the relative intensities of the signals and noises being discussed. The noise terms are the dashed lines, while the corresponding signal is shown as a solid line of the same color (with the total noise being the red dashed curve). When the sample is greater than the noise criterion (here $I_s > \sqrt{I_s}$), then it is successfully amplified above all noise. However, if the sample signal is weaker than its self-noise, then although it is amplified above the background noise, it unfortunately remains below the noise introduced by the amplifier, and hence below the overall noise criterion. Thus samples whose intrinsic signal-to-noise make

them unmeasurable cannot be salvaged with X-amp; but weakly scattering samples obscured by strong background noise can be amplified into a measurable regime.

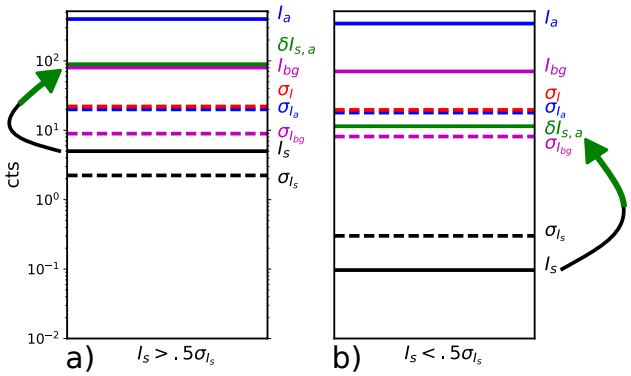

Fig. 1. A schematic of the amplification procedure, showing the relative intensities of the signal and noise terms. The noise terms are shown as dashed lines, while the corresponding signals are shown as solid lines of the same color. The total noise is shown as a dashed red line. (a) When the sample signal (solid black) is at least above its self-noise ($I_s > \sigma_s = \sqrt{I_s}$), the amplification procedure brings it above all noise terms (dashed lines). (b) However, when the sample signal is below its self-noise term, it can be boosted above the background noise (dashed purple) but it cannot be boosted above the amplifier's noise (dashed blue).

2. Amplifier Design

In designing a suitable amplifier, numerous structures were proposed. We investigate the simulated scattering of a few of these. We know that the intensity is related to the scattering cross section which is given by (Als-Nielsen & McMorrow, 2011):

$$I = \Phi_0 \tan^2\left(\frac{a}{R}\right)\frac{d\sigma}{d\Omega} \tag{1}$$

(2)

where Φ_0 is the flux (photons/s/m^2, assumed constant over the samples measured), a the size of a pixel (75μm for EIGER 4M) and R is the sample to detector distance (4.81 m). The scattering cross section, in the far field, is given by the Born

approximation (Als-Nielsen & McMorrow, 2011):

$$\frac{d\sigma}{d\Omega} = |r_0 \mathrm{F}(\vec{q})|^2 \quad (3)$$

$$\mathrm{F}(\vec{q}) = \int_V \delta\rho'(\vec{q}) e^{i\vec{q}\cdot\vec{r}} d\vec{r} \quad (4)$$

$$\delta\rho'(\vec{r}) = \rho'_s(\vec{r}) - \rho'_m(\vec{r}) \quad (5)$$

$$\rho'_{s,m} = \frac{f_{s,m} - |f'_{s,m}|}{f_{s,m}} \rho_{s,m} \quad (6)$$

where r_0 is the classical Thomson radius, ρ is the electron density and $\delta\rho$ is the effective electron density difference between the sample (s) and medium (m), which depends on the energy dependent dispersion correction f' (Als-Nielsen & McMorrow, 2011). Absorption is ignored due to the thin nature of the samples. Note, the absolute value is used due to the possible ambiguity in sign definition of f' (usually negative). The absolute scattering is not of importance so these will be ignored.

The simplest of these structures is a pinhole. The equivalent to this would be a gold post. The analytic structure factor of a pinhole of depth D and radius r is:

$$\mathrm{F}_{\mathrm{post}}(qR) = \int_V \delta\rho'(\vec{r}) e^{i\vec{q}\cdot\vec{r}} d\vec{r} \quad (7)$$

$$= 2\pi D\delta\rho' \int_0^R \mathrm{circ}(\frac{r}{R}) e^{i\vec{q}\cdot\vec{r}} d\vec{r} \quad (8)$$

$$= 2\pi DR^2 \int_0^R \delta\rho' \mathrm{circ}(\frac{r}{R}) e^{i(\vec{q}R)\cdot\vec{r}'} d\vec{r}' \quad (9)$$

$$= 2\pi R^2 D\delta\rho' \frac{\mathrm{J}_1(qR)}{qR} \quad (10)$$

$$\mathrm{circ}(r) = \begin{cases} 1, & r \leq 1 \\ 0, & r > 1 \end{cases} \quad (11)$$

where J_1 refers to the first order Bessel function of the first kind. Note that $\lim_{qR\to 0} \frac{\mathrm{J}_1(qR)}{qR} = \frac{1}{2}$ and thus $\mathrm{F}(qR = 0) = \delta\rho\pi R^2 D = \delta\rho V_{post}$. For no medium and negligible dispersion corrections, this is equivalent to the number of electrons in the sample, which is what is expected. The rings may be summed one by one. One ring is the difference of two posts:

$$\mathrm{F}_{\mathrm{ring}}(q, R_1 R_2) = \mathrm{F}_{\mathrm{post}}(qR_2) - \mathrm{F}_{\mathrm{post}}(qR_1) \quad (12)$$

where R_1 and R_2 are the inner and outer radii, respectively. A sum of rings is just computed by summing $\mathrm{F}_{\mathrm{ring}}$ over the appropriate rings, spaced d_s apart:

$$\mathrm{F}_{\mathrm{rings}}(q, R_1 R_2) \quad = \quad \sum_{i=1}^{N_{\mathrm{ring}}} \mathrm{F}_{\mathrm{ring}}(q, id_s - \frac{\Delta R}{2}, id_s + \frac{\Delta r}{2}) \tag{13}$$

A plot of the comparison of the form factor of a post versus 5 rings is plotted in figure 2. Near the first order peak in the scattering of the rings, the scattering is a factor of 50 times stronger than the disc. The peak is at $\frac{2\pi}{d_s}$ (the inverse ring spacing). This parameter may be tuned to match the desired wave vector to amplify. The only way to increase the intensity of the disc at that q is to increase the radius (see the trend in figure 3). Thus for every disc of a fixed radius there always exists a ring that may scatter stronger in certain regions of reciprocal space. For this proof of principle experiment, it was more desirable to increase the scattering of our amplifiers as much as possible for one region in q in order to increase the number of samples that may be amplified. The final extent of the rings was chosen to be near 1μm in diameter.

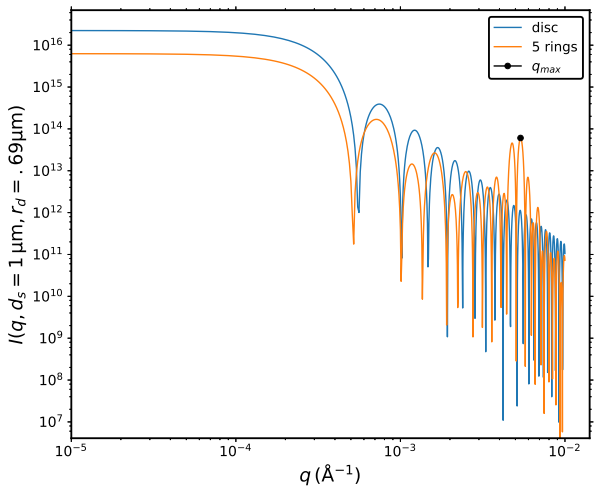

Fig. 2. The form factor of a disc versus a ring. The radius of the disc r_d is made to match the outer edge of the ring: $r_d = r_0 + d_s * N_{\mathrm{rings}} + \frac{dr}{2}$.

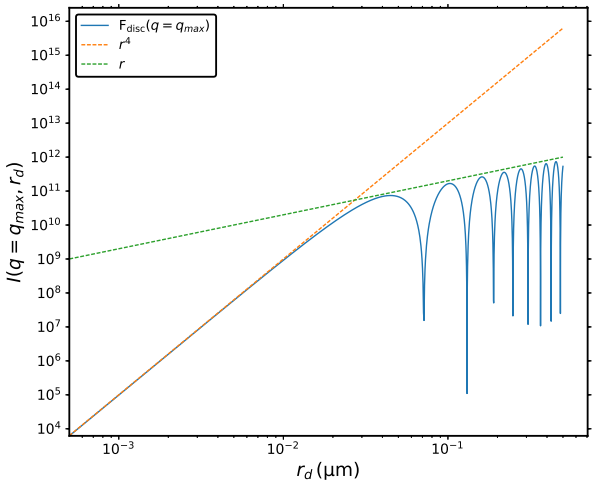

Fig. 3. A plot of the scattering of a disc versus radius R at wave vector q_{max}. Decreasing the radius decreases the scattering. When the radius reaches $\frac{2\pi}{2r} = q_{max}$, the intensity increase becomes less favorable, trending as R as opposed to R^4.

Anisotropic amplifiers were also considered. The anisotropy resulted in a loss of amplified scattering for all wave vectors ϕ but a slight increase in wave vectors q. The anisotropy is now sensitive to sample orientation and could be an interesting amplifier to use when a certain orientation is desired. A simulation of rings and chevrons with the same extent are found in figure 4. These were not chosen since they require the sample to have a specific symmetry and orientation in order to detect a signal.

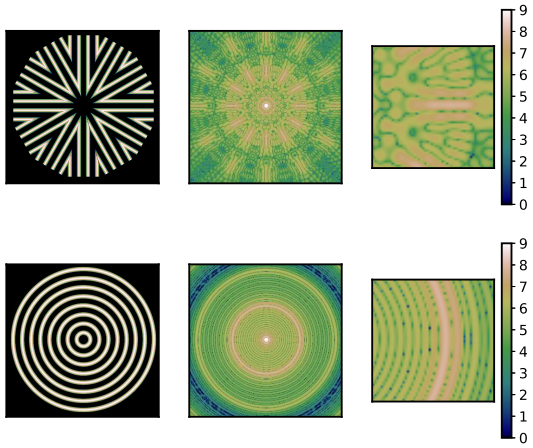

Fig. 4. Top row left to right: A plot of a real space image of chevrons, the simulated scattering, and a zoom. Bottom row left to right: A plot of the real space image of rings, the simulated scattering and a zoom. Both peak similar in scattering. The rings cover all azimuth ϕ whereas the chevrons do not, but cover slightly larger q.

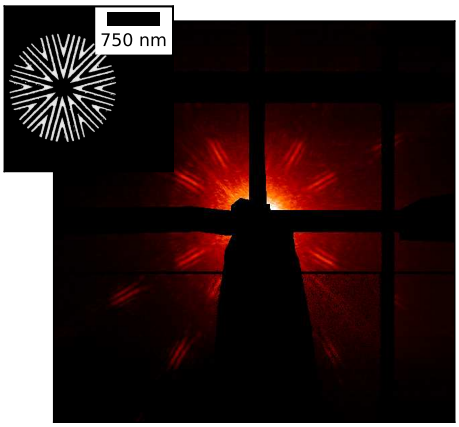

Fig. 5. A plot of the chevron pattern and its scattering (log scale).

3. Maximum longitudinal displacement

There is a strong advantage to minimizing the longitudinal displacement between the sample and amplifier. In particular, when the longitudinal displacement is large,

the $\Delta\vec{r}$ vector has a significant component along the beam direction. The resulting interference term of course oscillates along this displacement vector. As a result, the measured interference pattern will be 'non-uniform,' with different apparent fringe periodicities in different parts of the image. This is simply due to the intersection between the curved surface of the Ewald sphere, and the (highly longitudinal) interference oscillation.

Figure 6 shows an example of this effect, obtained by co-aligning a sample and amplifier fabricated on two separate substrates. By aligning both close to the beam center, they occupy the same coherence volume and interfere coherently; this can be confirmed by noting the appearance of fringes in the total scattering pattern. However, by increasing the longitudinal displacement between the sample and amplifier, the spacing and direction of the fringes become non-uniform across the detector image. However, one can still clearly see the enhanced visibility of the symmetry of the sample where the fringes are visible. Angular correlation analysis on this data still extracts the symmetries of the sample. This is confirmed with simulations described further along this document.

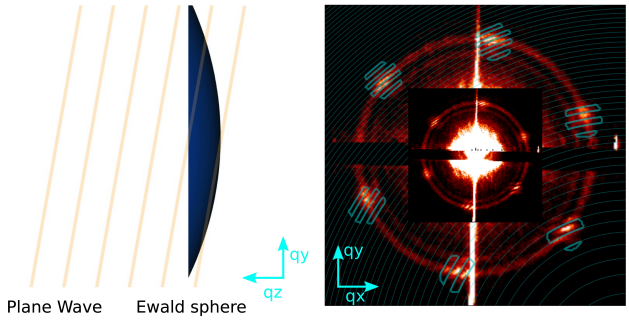

Fig. 6. Example of the total scattering (right) for a sample and amplifier separated by $\approx 450\,\mu$m in the longitudinal direction (along the beam direction). The observed fringes arise from the intersection of the Ewald sphere (left, blue) and the interference pattern, which can be thought of as a plane wave, $e^{i\vec{q}\cdot\Delta\vec{r}}$ (beige planes). When the displacement vector has a substantial longitudinal component, this intersection gives rise to concentric circles of scattering intensity. In the right image, the contours of the peaks in the frequency modulation are overlaid as cyan curves. For ease of viewing, only every second contour is plotted. These effects can also give rise to interference fringes oscillating with a higher frequency that would be predicted if considering only the x and y components of the displacement.

In X-amp, the highest-frequency components are due to the phase term in Equation 9 of the main text. The sampling in reciprocal-space is determined by the experimental setup:

$$q_{x,y} = \frac{2\pi}{\lambda}\sin\left(\tan^{-1}\left[\frac{N_{\rm pix}d_{\rm pix}}{R_{\rm det}}\right]\right) \approx q_{SAXS} \tag{14}$$

$$\Delta q_{x,y} \approx \frac{2\pi}{\lambda}\frac{d_{\rm pix}}{R_{\rm det}} \tag{15}$$

$$q_z = \frac{2\pi}{\lambda}\left(1-\cos\left(\tan^{-1}\left[\frac{N_{\rm pix}d_{\rm pix}}{R_{\rm det}}\right]\right)\right) \approx \frac{2\pi}{\lambda}\left(\frac{N_{\rm pix}d_{\rm pix}}{R_{\rm det}}\right)^2 \tag{16}$$

$$\Delta q_z \approx \frac{4\pi}{\lambda}\frac{N_{\rm pix}d_{\rm pix}^2}{R_{\rm det}^2} = 2q_{\rm SAXS}\frac{d_{\rm pix}}{R_{\rm det}} \tag{17}$$

$$q_{\rm SAXS} = \frac{2\pi}{\lambda}\frac{N_{\rm pix}d_{\rm pix}}{R_{\rm det}} \tag{18}$$

where λ is the x-ray wavelength, $d_{\rm pix}$ the pixel size ($75\,\mu$m in our experiment), $N_{\rm pix}$ the number of pixels away from the the $q=0$ center on the detector, $R_{\rm det}$ the sample-to-detector distance, and $q_{\rm SAXS}$ is the wave vector assuming the small angle approximation. The requirement of sampling 4 points per period entails (where $r_\perp$ is the

direction perpendicular to the incoming beam, in the detector plane):

$$\frac{2\pi}{\Delta r_\perp} > \Delta q_\perp \tag{19}$$

$$\Delta r_\perp < \frac{1}{4}\lambda\frac{R_{det}}{d_{pix}} \tag{20}$$

$$\frac{2\pi}{\Delta z} > \Delta q_z \tag{21}$$

$$\Delta z < \frac{1}{4}\frac{\pi}{q_{\rm SAXS}}\left(\frac{R_{\rm det}}{d_{\rm pix}}\right). \tag{22}$$

For example, for the setup described herein, with $R_{det} = 4.81$ m, $d_{pix} = 75$ μm, wavelength $\lambda = 1.4\,$Å, and maximum wave vectors of $q_{\rm SAXS} = .01\,$Å^{-1} (resolutions down to 62 nm), the restrictions are $\Delta r_\perp \approx 2\ \mu$m and $\Delta z \approx 500\,\mu$m. These restrictions can be relaxed by either reducing the detector pixel size or increasing sample-detector distance. This is done at the cost of a reduction of flux per pixel. It is important then to ensure that the signal-to-noise criteria of the sample and amplifier are still met.

4. Simulations

The planar interference terms were simulated by Fourier transforming the projection of the density. The scattering is again given by equation 4. We ignore the scaling constants and replace them by an arbitrary constant C and consider only the form factor:

$$I = C|F(\vec{q})|^2 \tag{23}$$

$$F(\vec{q}) = \int \delta\rho(\vec{r})e^{i\vec{q}\cdot\vec{r}}d\vec{r} \tag{24}$$

At small angle and small longitudinal displacements, we can approximate $e^{i\vec{q}\cdot\vec{r}} \approx e^{i\vec{q}_\perp\cdot\vec{r}} = e^{i(q_x x+q_y y)}$:

$$F(\vec{q}) \sim \frac{1}{V}\int_A\left(\int_z \delta\rho(\vec{r})dz\right)e^{i\vec{q}\cdot\vec{r}}d\vec{r} \tag{25}$$

$$= \frac{1}{A}\int_A \rho_\perp(x,y)e^{i\vec{q}\cdot\vec{r}_\perp}d\vec{r}_\perp \tag{26}$$

$$\delta\rho_\perp = \frac{1}{\Delta z}\int_z \rho(x,y,z)dz \tag{27}$$

where A is the area and $\delta\rho_{\perp}$ is the projection of the density onto the xy plane.

The simulations are discretized into a finite grid. The projection of the density was obtained from either computational modeling or by taking the SEM images. Both yielded similar results. The results using the computed images are not limited by the resolution of the SEM images taken and so thus will be considered here.

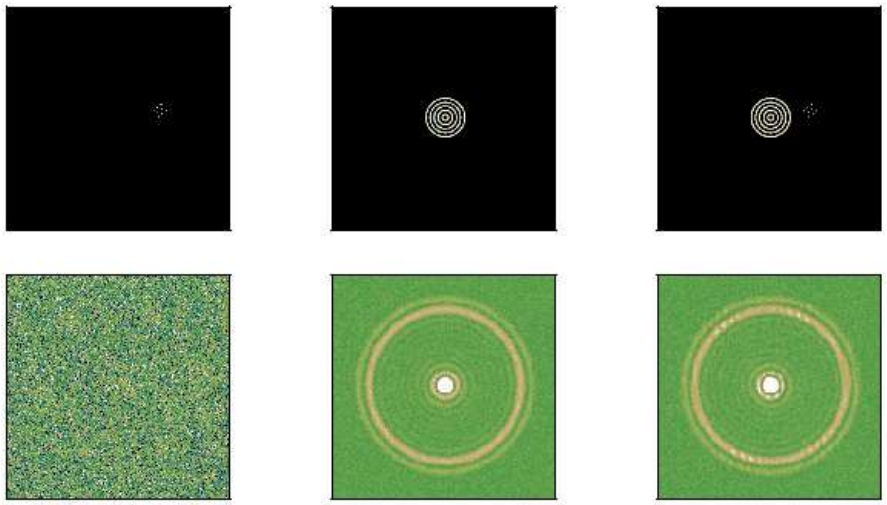

Fig. 7. A plot of the images (top row) and their caclulated scattering (bottom rown) for the sample on its own (left), the amplifier (middle) and their interference (right).

A sample image of the simulated images may be seen in figure 7. A 3x3 hexagonal arrangement of dots was used with a set of 5 concentric rings. The spacing of the concentric rings was set so that the peak in the scattering from the rings matched that of the sample. The circular averaged structure factors are seen in figure 8 where it is clear that the peak in the scattering of the rings coincides that of the sample. The scattering intensity was also rescaled so that the average count rate at the ring which the sample and amplifier coincide are approximately 50 counts for the sample and 4000 for the amplifier. Note that the peak in figure 8 is lower due to the circular average of the scattering peaks.

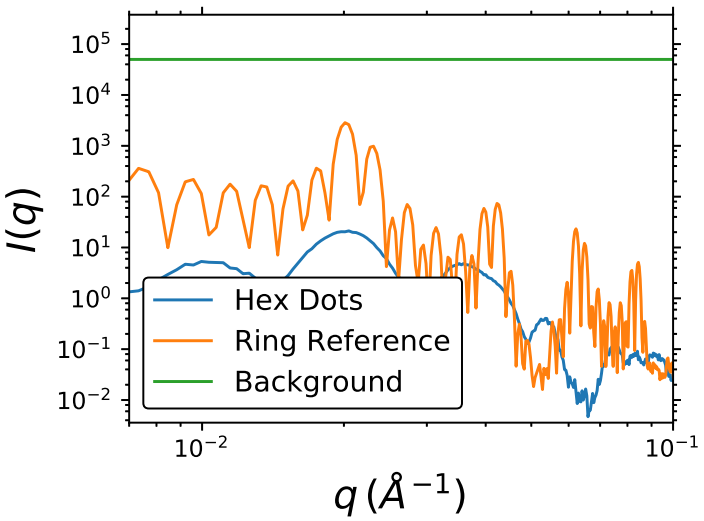

Fig. 8. A plot of the azimuthally averaged structure factors

Next, a background of 4×10^4 cts was added. The scattering was computed for 15 different combinations of sample, amplifier and sample and amplifier scattering. In each combination, the sample, amplifier were independently rotated. In the case of the sample and amplifier, the sample was also randomly translated. The scattering was computed by a 2D Fourier transform using the python numpy library.

The correlation around the ring of maximum scattering was computed and the results are seen in figure 9. The blue curve in each plot is the correlation of the sample without background. The correlation of the sample on its own $\mathrm{C}_{1,s}(\Delta\phi)$ is not visible, nor is the first order correlation of the sample and amplifier $\mathrm{C}_{1,s+a}(\Delta\phi)$. However, the second order correlation $\mathrm{C}_{2,s+a}(\Delta\phi)$ is clearly visible. The curves were subtracted by their average $\langle C\rangle_{\Delta\phi}$ and normalized: $\mathrm{c}(\Delta\phi) = \frac{\mathrm{C}(\Delta\phi)-\langle \mathrm{C}\rangle_{\Delta\phi}}{A}$, where A is a normalization constant. From appendix B, assuming the sample scattering is much smaller than the amplifier scattering and subtracting the average background, the

second order correlation function should be:

$$C_2(\Delta\phi) = 4\bar{I}_{tot}^4 X_a^2 X_s^2 c_s(\Delta\phi) c_a(\Delta\phi) \quad (28)$$

$$X_s = \frac{\bar{I}_s}{\bar{I}_{tot}} \quad (29)$$

$$X_a = \frac{\bar{I}_a}{\bar{I}_{tot}} \quad (30)$$

$$\bar{I}_{tot} = \bar{I}_{bg} + \bar{I}_s + \bar{I}_a. \quad (31)$$

We thus normalize the computed correlation function from the simulation by the expected amplitude $A = \bar{I}_{tot}^4 X_a^2 X_s^2$. With this normalization, we see that the theoretical (blue) and simulated curves (magenta) agree (rightermost plot in figure 9). This result confirms that the second order correlation $C_{2,s+a}(\Delta\phi)$ function does indeed show the symmetry of the sample, and that its amplitude is what is expected from Appendix B.

Finally, the approximate expected signal to noise **of the image itself** is calculated for the sample with background, interference term with background and the theoretical limit of a very large amplifier, in figure 10, which are again:

$$SN_{sam} = \frac{I_s}{\sqrt{I_{bg} + I_a + I_s}} \quad (32)$$

$$SN_{sam,nobg} = \frac{I_s}{\sqrt{I_a + I_s}} \quad (33)$$

$$SN_{interference} = \frac{2\sqrt{I_s I_a}}{\sqrt{I_{bg} + I_a + I_s}} \quad (34)$$

$$SN_{theoreticallimit} = \frac{2\sqrt{I_s I_a}}{\sqrt{I_a + I_s}} \quad (35)$$

Note the theoretical limit of the interference term will always be twice that of the sample.

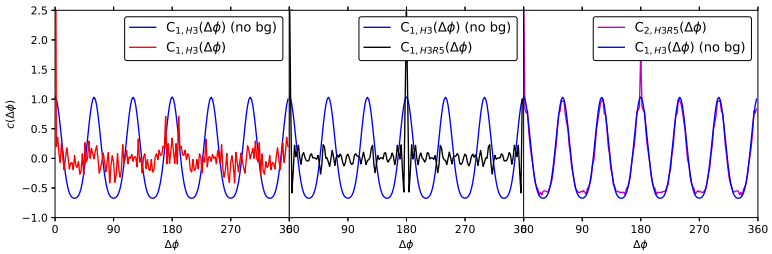

Fig. 9. A plot of the correlation functions for the sample on its own (left) with (red) and without (blue) background, the first order correlation function (middle) of the interference term (black), compared with the sample on its own witout background (blue) and the second order correlation function (right) of the interference term (magenta) compared with the correlation function of the sample on its own (blue).

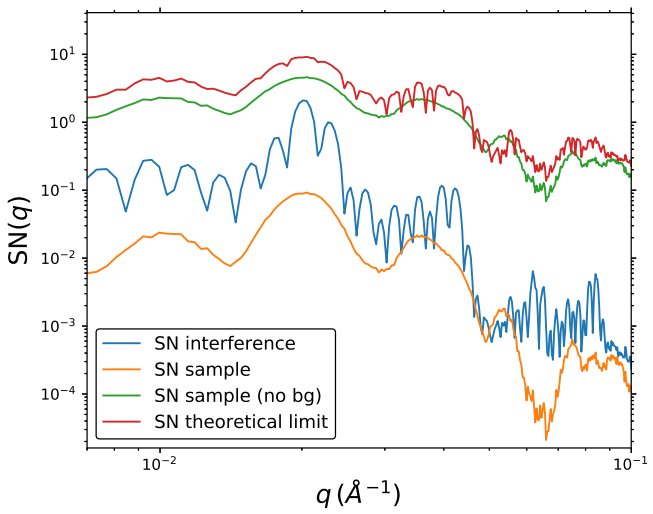

Fig. 10. A plot of the signal to noise of the sample, the interference, and the theoretical limit (in limit of large and perfect amplifier).

4.1. Simulations with planarly displaced samples

In the three-dimensional reciprocal-space, the interference term is modulated by:

$$e^{i\vec{q}\cdot\Delta\vec{r}} = e^{i(q_x\Delta x+q_y\Delta y+q_z\Delta z)} \tag{36}$$

where:

$$q_x = \sin 2\theta \cos\phi \tag{37}$$

$$q_y = \sin 2\theta \sin\phi \tag{38}$$

$$q_z = (1-\cos 2\theta) \tag{39}$$

In small-angle scattering, the q_z component is very small (at least two orders of magnitude smaller than the $q_{x,y}$ components, for conditions examined here). Thus, the q_z component is normally neglected. However, if the longitudinal Δz is much larger than

the Δx and Δy displacements, the product $q_z \Delta z$ may add a non-negligible contribution to the phase. This effect can be modeled.

To demonstrate the validity of the correlation analysis, the analysis was performed on simulated data. The simulations were performed again adding planar displacement. The planar displacement was added by adding an extra phase term to the simulated scattered field terms:

$$I \quad = \quad |F_s|^2 + |F_a|^2 + \left(F_s F_a^* e^{i(q_x \Delta x + q_y \Delta y + q_z \Delta z)} + \text{c.c.} \right).$$

The amplifier subtracted scattering can be seen in figure 11, for one instance of a simulated 5x5 array and amplifier. The sample was placed randomly between 1.5 μm-2 μm from the center of the reference. The dimensions of the sample and reference were the same as seen in the SEM images.

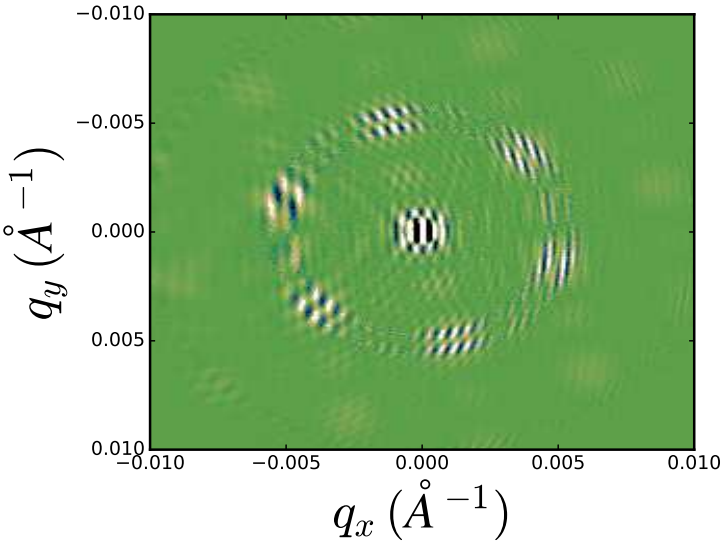

Fig. 11. A plot of the reference subtracted scattering.

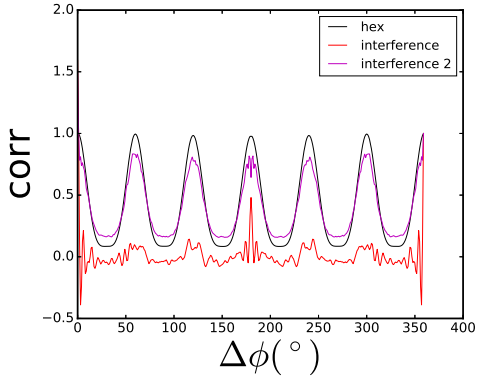

Fig. 12. A plot of the correlations at the 1st order peak for the sample on its own (black), sample with reference (red) and the 2nd moment correlation function of the sample with the reference (magenta).

The correlation analysis presented above is robust with respect to non-uniform oscillations throughout the image, provided that one averages over an ensemble of sample realizations with different in-plane (x and y) displacement amounts. Even though the interference fringes may not be uniform within a particular image, their apparance throughout the image is still a representation of the sample scattering; correlating between regions of high variance (where the fringes appear) will recover the sample symmetry. Experimentally, the high-frequency oscillations that can be introduced by the longitudinal displacement can, however, reduce data quality. In the limit of very high-frequency oscillations, the detector pixel resolution will become insufficient. Thus, there is a clear advantage to minimizing the sample-amplifier longitudinal displacement. Experimentally, we find that a modest and readily acheivable displacement (100 to 500 μm) yields interference fringes of sufficient visibility to be amenable to analysis.

4.2. Simulation of the Boost Factor

To save on computation time, the simulation of the boost factor for the angular correlations was simplified to a 1D example, which is here assumed to be a ring of constant wave vector magnitude q. The sample chosen was a 6 fold symmetric arrangement of Gaussian peaks:

$$E_s(\phi, \vec{q}, \vec{r}_s, \phi_0, \sigma_\phi) = \sqrt{A_s} e^{i\vec{q}\cdot\vec{r}_s} \sum_{j=1}^{6} e^{-\frac{(\phi+\frac{2\pi}{6}j-\phi_0)^2}{2\sigma_\phi^2}}$$

where $\sigma_\phi = .08$rad, $\sqrt{A_s}$ is the maximum amplitude of the electric field and $\vec{r}_s$ is the position of the sample, consistent with the Born approximation (Als-Nielsen & McMorrow, 2011). The intensity (ignoring constant factors) is:

$$I_s(\phi, \phi_0, \sigma_\phi) = |E_s|^2 = A_s \left(\sum_{j=1}^{6} e^{-\frac{(\phi-\phi_0)^2}{2\sigma_\phi^2}} \right)^2 .$$

The maximum intensity is A_s. The field of the amplifier is chosen to be:

$$E_a(\phi, \vec{q}, \vec{r}_a) = \sqrt{A_a} e^{i\vec{q}\cdot\vec{r}_a}$$

where the intensity of the amplifier is:

$$I_a(\phi, \phi_0, \sigma_\phi) = |E_a|^2 = A_a.$$

The intensity of the amplifier is then A_a. When the amplifier and sample coherently interfere, the scattered fields are superposed:

$$E = E_s + E_a.$$

and their intensity:

$$I = |E_s + E_a|^2. \tag{40}$$

$$= |E_s|^2 + (E_s E_a^* e^{i\vec{q}\cdot\Delta\vec{r}} + \text{c.c.}) + |E_a|^2 \tag{41}$$

$$\Delta\vec{r} = \vec{r}_s - \vec{r}_a \tag{42}$$

where c.c. stands for complex conjugate. This term fluctuates between $(\sqrt{A_s}+\sqrt{A_a})^2$ and $(\sqrt{A_s}-\sqrt{A_a})^2$. In order to simulate the system, values for $\vec{q}$ and $\Delta\vec{r}$ must be chosen. The wavevector magnitude q is in the regime of $.001-.01\text{Å}^{-1}$, and so $q=.005$ was chosen. The sample amplifier distance $|\Delta\vec{r}|$ was chosen to range from 0nm − 800nm. Finally, an incoherent background was applied to the sample and interference intensities:

$$I_{\text{noamp}} = |E_s|^2 + A_{bg} \tag{43}$$

$$I_{\text{amp}} = |E_s|^2 + (E_s E_a^* e^{i\vec{q}\cdot\Delta\vec{r}} + \text{c.c.}) + |E_a|^2 + A_{bg} \tag{44}$$

$$\Delta\vec{r} = \vec{r}_s - \vec{r}_a \tag{45}$$

The defining parameters for the unamplified scheme simulation (equation 43) are A_s, the sample maximum intensity, σ_ϕ, the width of the Gaussian peaks, ϕ_0, the orientation of the sample and A_{bg}, the background intensity. The orientation of the sample is randomly varied whereas the width is kept fixed. For the amplified scheme, the defining parameters are the same as that for the unamplified scheme, as well as A_a, the amplifier intensity, and $\Delta\vec{r}=(\Delta x,\Delta y,0)$ the sample-amplifier distance. The latter is varied randomly such that $0\text{nm} \leq |\Delta\vec{r}|^2 = \sqrt{\Delta x^2+\Delta y^2} \leq 800\text{nm}$. The combination of these parameters results in a simulation with free parameters A_a and A_{bg}. The final intensity is computed by sampling from a Poisson distribution whose intensity is defined by the simulated intensity in the previous step.

The correlation of the intensity on each simulation of the unamplified scheme is fit to the expected correlation function assuming no noise. The noise is defined as the χ^2 difference between the fit and the sample, and the signal is defined as the standard deviation of the fit. The same is performed for the amplified scheme, except that the second order correlation function is taken. The boost factor is then the ratio of these two values, computed as in figure 5 of the original document.

Parameter	Value or Range	fixed, random, varied
A_s	10 cts	fixed
σ_ϕ	.8 rad	fixed
ϕ_0	$0 - 2\pi$ rad	random
A_a	$10 - 10^4$ cts	varied
A_{bg}	$1 - 10^4$ cts	varied

5. Location of sample

When conducting these experiments where some samples may not be visible above background, sample location is crucial. A system was devised where patterns of successively weaker scattering and more localized center of mass were patterned. The layout was as can be seen in figure 13. Since the structures are small to begin with (the whole grid being 1.28mm in extent), a large "L" shaped pattern of gold is placed on the pattern. This shape is visible by eye and allows the sample to be placed in the correct orientation which is crucial. Next, the sample is carefully centered to within $500\mu m$ by eye. The xray beam is scanned along the sample in 10 micron increments at a 10 second exposure by translating the sample until a signature from the grid lines (in the figure) is found. When found, the xray is scanned until a region of interest centered on one of the diffraction peaks is maximized. This is done in the vertical and transverse directions. The sample is often not perfectly horizontal but tilted (in the directions transverse to the incoming beam). The tilt is also measured by precisely calculating it from the peaks (there is a 1.5° tilt in the image shown). The tilt is taken into account when translating the motors across the sample.

This accuracy is often not enough for the large number of patterns per substrate. In order to improve the accuracy, samples localized in both transverse directions and of fairly strong and known scattering are placed throughout the sample (red squares in figure 13). The scattering of the sample is strong enough to be observed in a 1 second exposure but not so strong that some of its scattering may be detected when on a neighbouring sample. This re-optimization of position is performed whenever the

beam is moved more than 6 spaces ($240\mu m$) in the x direction and 2 spaces ($80\mu m$) in the y-direction.

The location the lithographic structures fabricated by electron beam lithography is accurate to within subnometer resolution. The amplifier structures were scanned with 500 nm step size at the beam line. The resolution of the stage motors is 50 nm. With interpolation, the samples were then centered with an accuracy better than 500 nm. For a Gaussian beam of standard deviation of 5 μm, this is sufficient.

Finally, prior to measurement, each sample considered in this paper was measured with SEM. The samples were all located and found to be produced as specified.

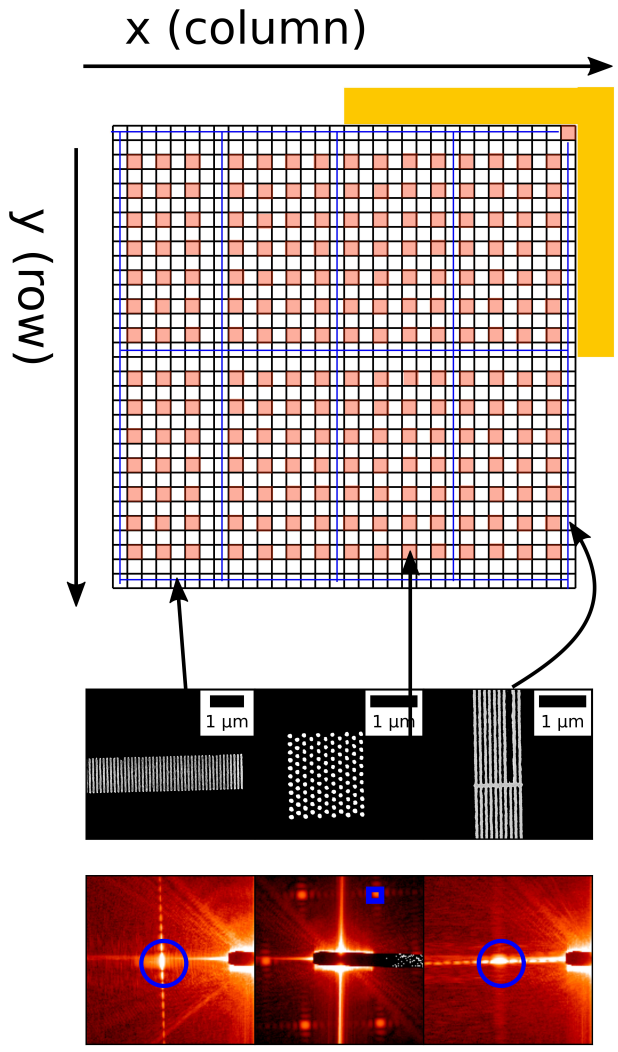

Fig. 13. The schematic of the lithographically patterned structures. The black lines are meant only to serve as a guide to the eye. Each sample is located on a 32x32 square grid of 40μm pitch so that when the beam is centered on a sample, is located at least 8 standard deviations away for a Gaussian beam of standard deviation 5μm. The blue lines refer to grid lines that are known to scatter strongly. In the regions of red squares, a strongly scattering sample, an 11x11 hexagonal array of dots is placed. SEM images and the resultant scattering are shown below the schematic. The images are 60 second exposures of the diffraction of each sample. One may see imperfections in the grid lines, as can be seen in the rightermost SEM image. These artifacts affect the scattering, but do not change the expected unique signature.

6. Intensity

The intensity of a few structures is presented here in figure 14. One sees that the peak in scattering from the rings coincides with the first order peaks of the arrays of dots, as can be seen by the circularly averaged structure factor in the bottom right figure of figure 14.

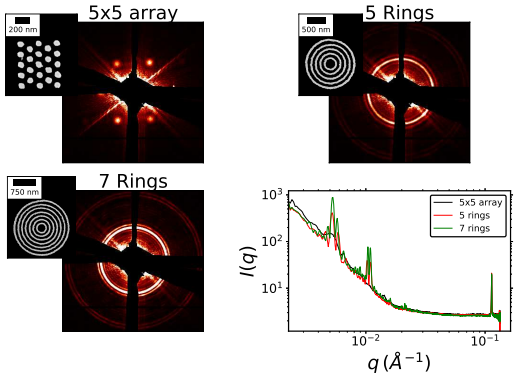

Fig. 14. The scattered intensity of a 60 second exposure of the hexagonal array (top left), 5 concentric rings (top right) and 7 concentric rings (bottom left), with the circularly averaged structure factors plotted (bottom right). The maximum of the concentric rings coincides with that of the 5x5 array.

7. Coherence

In order for the sample to be resolvable, there must be coherent interference among the samples in the scattering volume, and this interference must be sampled by at least 2 pixels per sample. The samples considered in this paper are not more than 2μm in extent. So to test these two criteria, a sample of this extent was measured. The sample chosen was a 22x22 array of dots of extent $\sim 2.6\mu m$. The highest frequency terms observed in the diffraction pattern are the intermodal peaks, which are related to a length scale of the extent of the sample, or $\sim 2.6\mu$m. One sees that at this length scale, the diffraction pattern is still well preserved. A larger sample, of 5.2 μm in extent was also measured. There is a clear loss in visibility of the fringes.

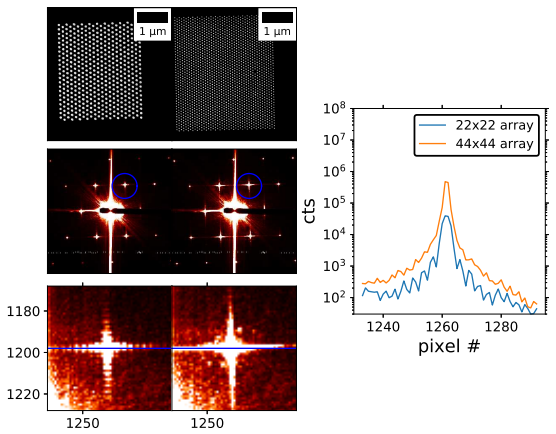

Fig. 15. A plot of the SEM images top row of the 22x22 array (left) and 44x44 array (right). The middle row is their measured scattering after a 60 second exposure, with the bottom row being a zoom in the corresponding highlighted blue boxes. Finally, a plot along the blue line in the zooms are plotted on the right. The fringes are well resolved for the 22×22 case, which confirms that interference effects on length scales of 22μm can be observed.

8. Correlation of sample on its own

A plot of the angular correlations of the a 3x3 hexagonal arrangement of dots and the amplifier structure was shown in figure 3 of the main paper. Here, we show the intensity along with the angular correlation of the same ring for the 3x3 array of dots on their own, in figure 16. The samples were confirmed to exist by SEM images (such as the one included in figure 16). The beam was centered with a precision better than 500 nm on the sample using the method described in section 5. Although the samples cannot be seen in the images, they can be seen through their correlations. In this case, the background was constant per measurement, and was determined by averaging measurements together. This is a different case from the results of Fig 4 of the main text, where the technique was not successful without the amplifier. In that case, the background changed per measurement, making background subtraction impossible.

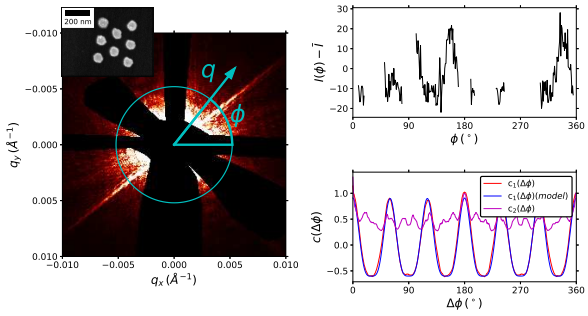

Fig. 16. A plot of the scattering of one of the 3x3 arrays left with its SEM image (top left), along with a plot the background subtracted intensity along the outlined cyan ring (plotted on the top left) and its first order and second correlation function(bottom right).

Acknowledgements

This research used resources of the Center for Functional Nanomaterials, and the National Synchrotron Light Source II, which are U.S. DOE Office of Science Facilities, operated at Brookhaven National Laboratory under Contract No. DE-SC0012704.

References

Als-Nielsen, J. & McMorrow, D. (2011). *Elements of modern X-ray physics*. John Wiley & Sons.